

Figure 1. (a): uGMRT 400 MHz blue contours with restoring beam $9.86'' \times 8.10''$, PA 87.28° overlaid on Pan-STARRS ‘r’ band optical image. The contours are placed at $(3,6,9,12,15) \times 35 \mu\text{Jy}/\text{beam}$. The X-ray and SZ centres of the cluster are marked in red as + and O, respectively, and radio galaxies near NE relic at cluster redshift are marked from A-E. (b): XMM X-ray contours in black and the uGMRT 400 MHz point source subtracted radio contours in blue overlaid on the uGMRT 400 MHz point source subtracted colour image with restoring beam $19.59'' \times 14.13''$, P.A 17.24° . The radio contours are placed at $(3,6,9,12,15) \times 42 \mu\text{Jy}/\text{beam}$. Subtracted compact sources near the diffuse emissions are highlighted with + in red.

Table 1. Properties of A2108 (Jensen & Pimbblet 2012; Planck Collaboration et al. 2014)

RA _{J2000}	15 h 40 m 07.96 s
DEC _{J2000}	+17° 53′ 55.2″
Mass (M_{500})	$3.01^{+0.38}_{-0.40} \times 10^{14} M_\odot$
Redshift (z)	0.0916
Dispersion velocity (σ_z)	750 km.s^{-1}
n_{H}	$2.38 \times 10^{20} \text{ cm}^{-2}$
Luminosity ($L_{\text{X}(0.1-2.4) \text{ keV}}$)	$1.97 \times 10^{44} \text{ erg.s}^{-1}$

uGMRT Low-MAss Galaxy Cluster Survey (GLOMACS) sample list. A brief of the available information regarding the cluster is presented in Table 1.

Notably, this is an X-ray under-luminous cluster in spite of having high ICM velocity dispersion (Jensen & Pimbblet 2012). The cluster hosts 3 brightest cluster galaxies (BCG) in the northern region itself (Crawford et al. 1999; Hogan et al. 2015). Recently, a steep spectrum radio relic ($\alpha = -2$) was discovered at the southwest of this cluster by Schellenberger et al. (2022). They also detected a shock ~ 200 kpc away in the southwestern direction from the radio relic. In this paper, we report important new findings from the deeper analysis of uGMRT band-3 and XMM-Newton X-ray archival observation of A2108.

We assume a Λ CDM cosmology with $\Omega_m = 0.3$, $\Omega_\Lambda = 0.7$ and $H_0 = 70 \text{ km s}^{-1} \text{ Mpc}^{-1}$. At the cluster redshift of $z = 0.0916$, $1''$ corresponds to 1.705781 kpc .

2 RADIO OBSERVATION

We observed the cluster with the GMRT during August 2021 (project code 40_088) as a part of uGMRT Low-MAss Galaxy Cluster Survey (GLOMACS) using band-3 with 195 min on-source time. 3C

286 was observed as flux and bandpass calibrator and 1419+064 as phase calibrator. The cluster was observed in both GMRT Software Backend (GSB) and GMRT Wideband Backend (GWB) modes with 16 sec and 2.6 sec integration time and 32 MHz and 200 MHz bandwidth, respectively. Both the GSB and GWB data were analyzed using the Source Peeling and Atmospheric Modelling (SPAM; Intema et al. 2009, 2017) pipeline. At first, the GSB data was pre-calibrated using SPAM. During the pre-calibration process, the flux density scale was set using Scaife & Heald 2012 model. Thereafter, bad data editing, several loops of self-calibration, and finally, direction-dependent calibration are performed. The output primary beam-corrected wide-field image was used as a sky model for our GWB data reduction. The 200 MHz bandwidth of GWB data was split into 6 smaller frequency chunks, each of 33 MHz. These sub-bands were calibrated and processed individually with SPAM using the reference sky model extracted from the GSB image. Multi-scale multi-frequency synthesis (MFS) map was made using WSClean v3.1.0 imager (Offringa & Smirnov 2017) in a joined-channel deconvolution mode using the calibrated visibilities from these 6 sub-bands.

We observed a faint diffuse emission signature near the Northeast of the cluster. To recover the whole structure and to achieve better image sensitivity, we used the available band-3 archival data of A2108 (Obs ID: 37_018) with 132 min on-source time. The archival GWB data was split into 6 sub-bands (33 MHz), and the pre-calibration was done using SPAM. Each of the sub-bands was then merged with the pre-calibrated sub-bands from our GLOMACS observation data. The merged sub-bands were then further processed with SPAM. The full-resolution image of the cluster created with the combined datasets using WSClean with Brigg’s robust 0.5 in Fig 1a (blue contours) shows both the faint diffuse emission as well as the compact sources present in the field. To remove the compact sources, we made high-resolution images for each of the merged sub-bands with Brigg’s robust -1 applying an inner uv-cut of $3 \text{ k}\lambda$ (corresponding to ~ 120 kpc at the cluster redshift) using CASA task *tclean*. The model vis-

Table 2. Best fit parameters of broken power law model (using PROFFIT) are listed below.

α_1	α_2	$r_{\text{sh}}(\text{arcmin})$	norm	Jump (C)	$\chi^2/D.o.f$	M_{SB}
-1.14 ± 0.28	2.50 ± 0.80	5.32 ± 0.05	$-2.85 \pm 0.05e - 05$	1.61 ± 0.27	1.50	$1.42^{+0.14}_{-0.14}$

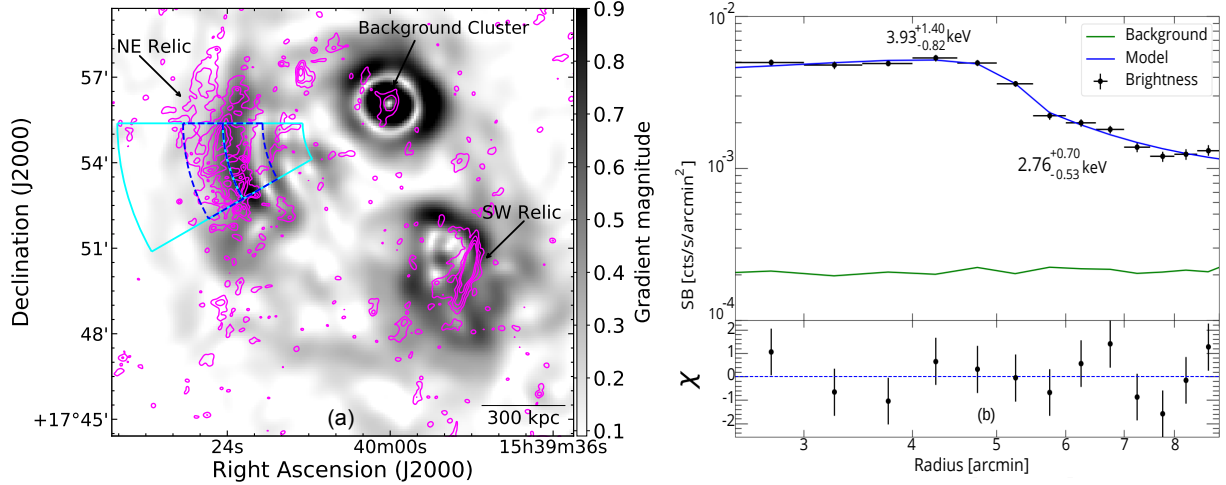


Figure 2. (a): Background subtracted GGM filtered XMM-Newton X-ray image of A2108 overlaid with uGMRT point source subtracted radio contours in magenta. The cyan and blue wedge regions show the area used to quantify the SB discontinuity and temperature discontinuity, respectively, and the central arc represents the jump location. (b): The SB profile over the wedge region, as shown in Fig. 2a and the respective temperatures over the regions.

ibilities from the high-resolution images were then subtracted from each of the sub-band visibilities. We made the point source subtracted final radio map of the cluster with Briggs’s robust 0.5, choosing the common uv-range of <20 k λ for all sub-bands and smoothing it with a Gaussian taper of $7''$ in WSClean (Fig. 1 b).

3 X-RAY OBSERVATION

We used archival XMM-Newton telescope observations (Obs ID: 0821810401) for this work. The data analysis was performed using the XMM-Newton Extended Source Analysis Software (XMM-ESAS), available in the SAS package. Further, we used Xspec v. 12.0 for X-ray spectral analysis. We performed a standard multi-step process to obtain clean EPIC data, spectral, and response files following the ESAS cookbook². Initially, the *cifbuild* task was utilized to construct the calibration index file, followed by the ingestion of the observational data using the *odfingest* task. Subsequently, the *epchain* and *emchain* tasks were applied to perform the necessary calibration and filtering on the EPIC-pn and EPIC-MOS data, respectively. We used full observation sets (PN, MOS1, and MOS2) except CCDs 3 and 6 of MOS1 were excluded as they suffered from damage from hits by micro-meteorites. Additionally, the *pn-filter* and *mos-filter* tasks were employed to apply specific filtering criteria for both instruments. We have used an off-source region, which is far away from the centre of the cluster, as background. Spectra were extracted using *evselect* task, and the background was scaled using *backscale* task. All the

spectra from PN, MOS1, and MOS2 were fitted simultaneously using XSPEC v12.0. The best-fitted temperature from the model Gaussian (0.47 keV) + Gaussian (1.75 keV) + constant*phabs*apec was noted for each region. The redshift, abundance (0.5 Z_{\odot}), and column density (n_H) were kept frozen during fitting.

4 RESULTS FROM RADIO OBSERVATION

Fig. 1a shows the GMRT band-3 full resolution radio contours of the cluster A2108 obtained with Briggs robust 0.5 (Briggs 1995) and restoring beam $9.86'' \times 8.10''$ PA 87.28° overlaid on Pan-STARRS ‘r’ band optical image. Two distinct diffuse emission features were observed in the cluster’s southwestern (SW) and northeastern (NE) periphery that do not have any obvious optical counterparts (see Fig. 1a). The brightest regions of SW and NE emissions are located at a distance of 550 kpc and 438 kpc away from the cluster X-ray centre, respectively. The SW diffuse structure was previously identified by (Schellenberger et al. 2022) as a 200 kpc long radio relic. However, there was no mention of the NE diffuse emission in previous studies. The location and morphology of the emission are indicative of a radio relic.

From our observation, we detect the SW relic with the largest linear size (LLS) of ~ 300 kpc and width of ~ 120 kpc. The diffuse emission at NE shows a patchy structure and spans over a region of 610 kpc \times 310 kpc. We estimated the flux density of the relics by measuring the total flux enclosed within 3σ contour (where $\sigma = 42 \mu\text{Jy}/\text{beam}$; Fig. 1b). We obtain the integrated flux density of 10.6 ± 0.8 mJy for the SW relic and 24.8 ± 1.8 mJy for the relic in the NE. Here, we note that the residual artefacts from the bright radio source D complicate the flux density measurement for the NE relic. Therefore,

² XMM-ESAS cookbook : <https://heasarc.gsfc.nasa.gov/docs/xmm/esas/cookbook/>

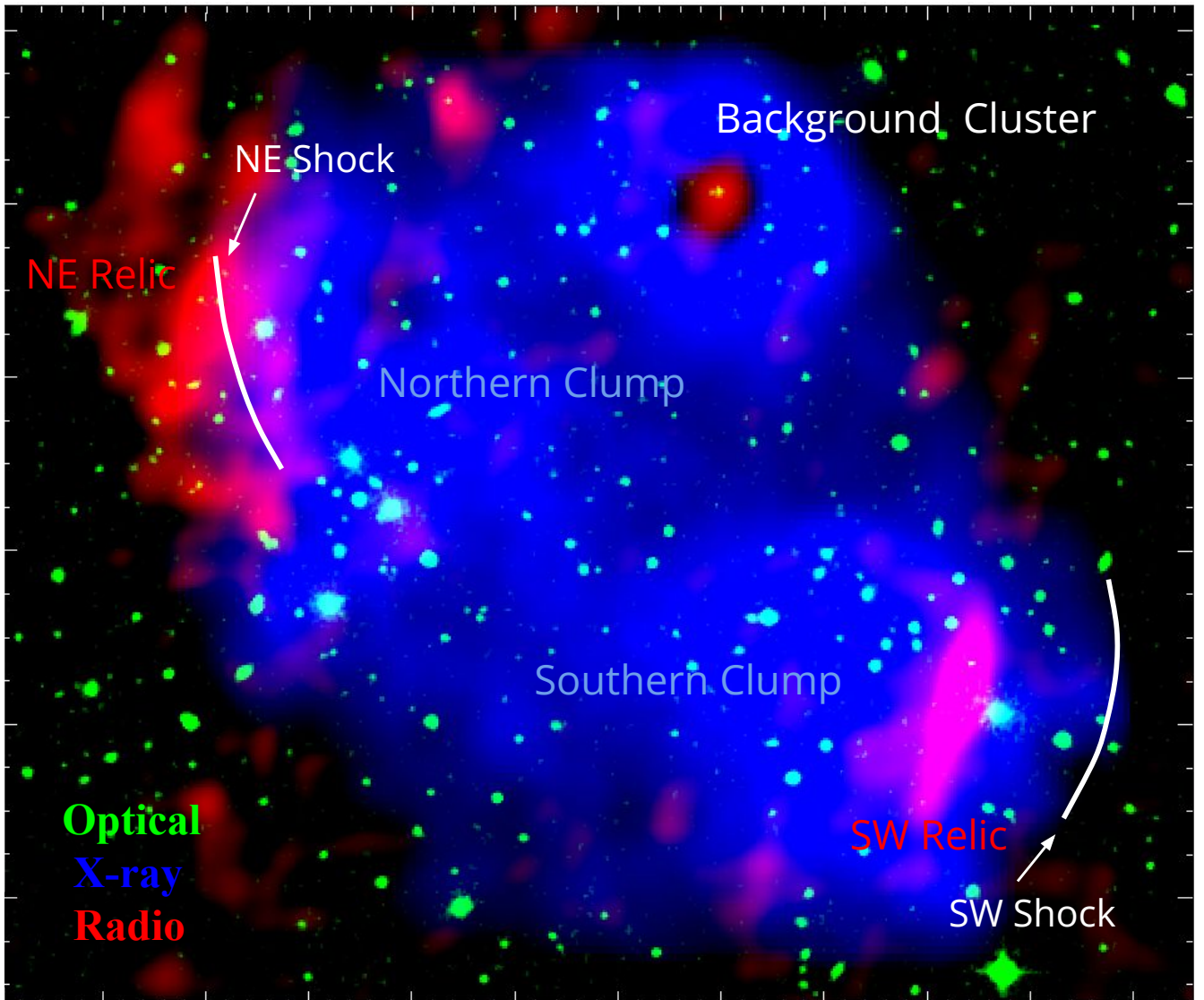


Figure 3. Colour composite image of A2108 showing Pan-STARRS ‘r’ band optical image in green, XMM-Newton X-ray in blue, and uGMRT point source removed radio image in red.

we also measured the flux density from the artefact-free brighter region falling under 6σ contours for the NE relic and found a flux density of 7.6 ± 0.6 mJy. The error in the flux density was estimated following van Weeren et al. (2021), where the map noise, uncertainty in absolute flux density calibration (we used 7% following Chandra et al. 2004), and uncertainty due to point source subtraction were taken into account. We have extrapolated the flux density of the relics to 1.4 GHz assuming a spectral index of -1.3 (typical for radio relics), and obtained a luminosity of $P_{1.4\text{GHz}|NE} = 1.05 \pm 0.07 \times 10^{23}$ W Hz $^{-1}$ and $P_{1.4\text{GHz}|SW} = 0.45 \pm 0.03 \times 10^{23}$ W Hz $^{-1}$. We see the surface brightness ($P_{1.4\text{GHz}}/LLS^2$) of the NE relic is lower (5.55×10^{17} W Hz $^{-1}$ Mpc $^{-2}$) compared to the SW relic (12.5×10^{17} W Hz $^{-1}$ Mpc $^{-2}$). This can be one of the possible reasons for the non-detection of the relic in the previous observations, and the better UV coverage and sensitivity achieved with our analysis aided in the detection.

5 RESULTS FROM X-RAY OBSERVATION

We created an X-ray map of the cluster (shown in blue in Fig. 3) using the XMM-Newton X-ray observation, combining data from PN, MOS1, and MOS2 in the energy range of 0.4–10.0 keV. The X-ray map reveals the presence of multiple substructures within it. As previously noted by Schellenberger et al. (2022), the northwestern clump in the surface brightness (SB) map of the cluster is attributed to a background cluster.

5.1 Edge detection

To locate any surface brightness discontinuity near the NE radio emission, we applied a Gaussian Gradient Magnitude (GGM) filtering method (Sanders et al. 2016). This technique estimates the gradient magnitude or the rate of change of intensity values in an image using a Gaussian filter. The Gaussian filter smooths the input image, which helps in emphasizing the large-scale structures and reducing noise. The gradient magnitude is then calculated using

derivative operators in the horizontal and vertical directions. The gradient magnitudes are then thresholded, where only pixels with intensity above a certain threshold value are retained. This further helps emphasize edges or boundaries with higher intensity while suppressing lower-intensity regions.

Fig. 2a represents the GGM-filtered image of A2108 overlaid with the radio contours. A sharp edge is seen at the northwest of the map due to the subtracted background cluster. Near the northeast, an arch-shaped SB edge can be observed coinciding with the diffuse radio emission. This sharp edge indicates discontinuities in the surface brightness, which can be caused by shock waves in the intracluster medium.

5.2 Surface Brightness and Temperature Discontinuity

Further, we looked for any discontinuities associated with SB and temperature near the edge location. We extracted the SB profiles from multiple annuli spread over the wedge region near the NE relic and fit the SB profiles with the broken power law using PROFFIT (Eckert et al. 2011). We noticed an SB discontinuity coinciding with the edge detected with GGM filtering (Fig. 2b). Moreover, a tentative jump in temperature from $3.93^{+1.40}_{-0.82}$ keV to $2.76^{+0.70}_{-0.53}$ keV was also noticed near the edge. The wedge and the jump locations have been highlighted as cyan arcs for the SB jump and blue arcs for the temperature jump in Fig. 2a.

Following Rahaman et al. (2022), the shock Mach numbers were calculated using the Rankine-Hugoniot shock jump conditions (Rankine 1870; Hugoniot 1887, 1889). The SB jump was calculated following the equation,

$$\frac{\rho_2}{\rho_1} = C = \frac{(1 + \gamma) \times M_{\text{SB}}^2}{2 + (\gamma - 1) \times M_{\text{SB}}^2} \quad (1)$$

where ρ_1 & ρ_2 are densities at pre and post-shock regions respectively. Considering $\gamma = 5/3$ for monoatomic gas, we get a shock Mach number from SB jump across the shock edge, $M_{\text{SB}} = 1.42^{+0.14}_{-0.14}$.

The Mach number from temperature jump was calculated following the equation

$$\frac{T_2}{T_1} = \frac{(5M_T^2 - 1)(M_T^2 + 3)}{16M_T^2} \quad (2)$$

where T_1 and T_2 are the pre-shock (upstream) and post-shock (downstream) temperatures, respectively. The Mach number from temperature jump was found to be $M_T = 1.43^{+0.12}_{-0.02}$.

6 DISCUSSION

Simulations show peripheral radio relics are to be generated at diametrically opposite sides due to cluster merger occurring in the plane of the sky (van Weeren et al. 2011a; Brüggén et al. 2012). However, there are only a few double relic systems reported so far, with most of the detection lying in clusters with $M_{500} \geq 5 \times 10^{14} M_{\odot}$ (Bonafede et al. 2017). So far, ~ 10 clusters have been detected with double relics in the low mass regime (Bonafede et al. 2017; Jones et al. 2023; Koribalski et al. 2023). In addition to the previously detected relic at the southwest of A2108 (Schellenberger et al. 2022), the detection of another diffuse structure at the northeastern periphery of the cluster reveals this cluster as a potential double relic system originated from the cluster merger-driven shocks. The X-ray surface brightness map of A2108 shows an elongation along northeast (NE) and southwest (SW), suggesting the potential merger axis. From the reported radius

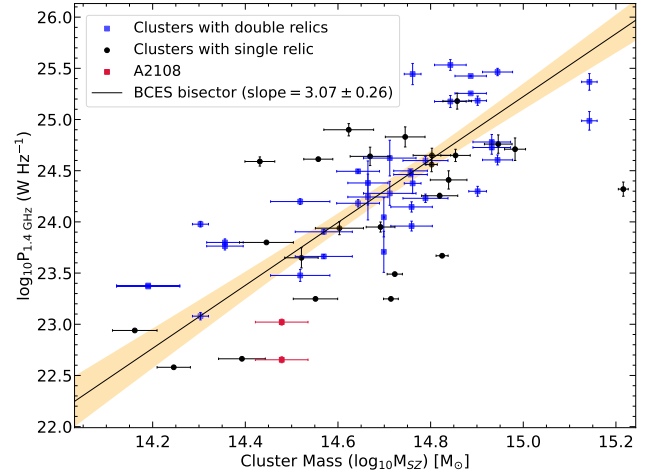


Figure 4. The 1.4 GHz power of radio relics available from literature (Kale et al. 2017; HyeonHan et al. 2020; Locatelli et al. 2020; Paul et al. 2021; Duchesne et al. 2021a; Lee et al. 2022; Chatterjee et al. 2022) is plotted against the host cluster mass. The blue squares show the double relics, and the black circles show the single relic systems. The red squares show the relics of A2108.

$r_{200} = 1.6$ Mpc (Jensen & Pimblet 2012), following Wen & Han (2013), we estimated the r_{500} to be ~ 1 Mpc for A2108 cluster. The relics of A2108 are also situated at a distance of ~ 1 Mpc in the sky plane and have a significantly different size ($300 \text{ kpc} \times 120 \text{ kpc}$ for the SW relic and $610 \text{ kpc} \times 310 \text{ kpc}$ for the NE relic). Correlation studies to understand the connection between host cluster mass and radio relic luminosity at 1.4 GHz have been performed previously (de Gasperin et al. 2014; Kale et al. 2017). In a recent work, Duchesne et al. (2021a) updated the scaling relation by incorporating double relics only. We revisited the correlation of radio relic power at 1.4 GHz with the host cluster mass for both single and double relics. Our sample comprises relics with known 1.4 GHz radio power from de Gasperin et al. (2014); Kale et al. (2017); HyeonHan et al. (2020); Locatelli et al. (2020); Paul et al. (2021); Duchesne et al. (2021a); Lee et al. (2022); Chatterjee et al. (2022). We used the Bivariate Estimator for Correlated Errors and Intrinsic Scatter (BCES) method to perform a linear regression on $P_{1.4 \text{ GHz}}$ and M_{500} . BCES accounts for errors in both the dependent and independent variables and for the intrinsic scatter of the data and thus is a robust approach. The scaling relation, $\log(P_{1.4 \text{ GHz}}) = A \log(M_{500}) + B$, yielded best-fit parameters $A = 3.07 \pm 0.26$ and $B = -20.86 \pm 3.88$, consistent with estimates incorporating the clusters with double relics (Duchesne et al. 2021a). We see that the NE relic is ~ 3 times under-luminous, and the SW relic is ~ 9 times under-luminous than what is expected from the relic mass-luminosity correlation.

Additionally, we compared the radio power and the LLS of the relics with the other relics. In Figure 5, we see that both the relics, especially the SW relic, are quite under-luminous compared to most of the double relic systems. The LLS of double relics generated in binary cluster merger roughly scales with the sub-cluster masses as shown by van Weeren et al. (2011a). However, it is important to consider the influence of the local environment in the relic formation and potential observational biases introduced due to projection effects (van Weeren et al. 2011b; Jones et al. 2021; Lee et al. 2022). Despite the fact that the sub-clusters of A2108 have comparable masses (Schellenberger et al. 2022), the LLS and breadth of the NE relic are significantly different (larger by a factor of two and three,

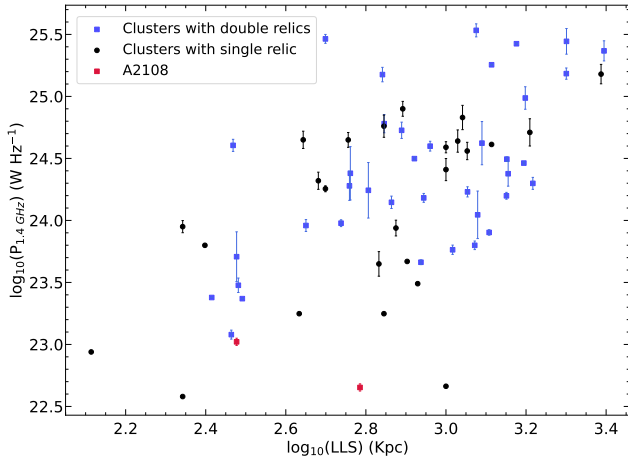


Figure 5. The 1.4 GHz power of radio relics available from literature (Kale et al. 2017; HyeongHan et al. 2020; Locatelli et al. 2020; Paul et al. 2021; Duchesne et al. 2021a; Lee et al. 2022; Chatterjee et al. 2022) is plotted against the relic LLS. The blue squares show the double relics, and the black circles show the single relic systems. The red squares show the relics of A2108.

respectively) compared to the SW relic. Moreover, the surface brightness ratio of the two relics is also not close to unity, as seen for most of the double relic systems Lee et al. (2022). These factors indicate the relics may not have the same origin. While the origin of the SW relic could be justified by the passage of shock front (Schellenberger et al. 2022), the morphology of the NE relic is suggestive of the influence of other secondary factors in the origin of the relic.

The X-ray SB map of the cluster also reveals interesting features in the ICM of A2108. Two X-ray bright sub-clusters at NE and SW and a faint X-ray emitting region between them, possibly from the trailing material of the sub-clusters, can be observed in Fig. 3. The low radio luminosity of the NE relic could be explained by the presence of a weak shock ($\mathcal{M}_{\text{SB}} = 1.42^{+0.14}_{-0.14}$) detected near the relic from X-ray analysis. Interestingly, this shock and the previously detected shock 200 kpc away from the SW relic (Schellenberger et al. 2022) appear in non-diametrically opposite directions (Figure 3), indicating a complex merger geometry. The cluster X-ray peak is sensitive to density, whereas the SZ peak is sensitive to pressure along the line of sight. Therefore, an offset is expected for merging clusters (Molnar et al. 2012; Zhang et al. 2014). However, the offset of the Peaks observed in A2108 (Fig. 1a) is roughly perpendicular to the merging axis, which is unusual given the cluster merging axis in the NE SW direction. The misalignment observed in optical galaxy density and the X-ray clumps also hint towards a non-linear merger axis (Schellenberger et al. 2022). We hypothesize that this feature can be observed due to an off-axis merger. Previously, off-axis merging has been predicted for galaxy clusters for instance, A115 (Hallman et al. 2018; Lee et al. 2020) and A141 (Caglar 2018). Interestingly, both A115 and A141 both host diffuse radio emission. Whereas A115 was reported to host a single radio relic (Govoni et al. 2001) with also a shock detected at the relic location (Botteon et al. 2016), A141 was reported to host a radio halo (see e.g. Duchesne et al. 2021b).

The brighter emission of the NE relic is also slightly misaligned with the shock front. Moreover, the NE relic is more expanded in the shock downstream region, which is peculiar to be formed by the DSA mechanism and considering the low Mach number detected via X-ray observation. There are multiple radio galaxies near the NE relic (highlighted with red ‘+’ in Fig. 1b). However, due to the lack of spectroscopic redshift information for the host galaxies, cluster

membership cannot be ascertained. Apart from the BCGs, we find the radio galaxy E with a possible optical host (SDSS J154017.98+1753; $z = 0.09104$) situated within 27 kpc distance at sky plane. No optical host was found for galaxy D. The re-energisation of the old electron population from these galaxies possibly has played a crucial role in the generation of the NE relic. The stronger evidence in favour of this scenario comes from the presence of patchy morphology of the relic. However, a detailed radio spectral index study would be required to shed more light on the particle acceleration phenomena near the relics.

7 CONCLUSION

In this paper, we report the discovery of a new relic in the northeast of low-mass galaxy cluster A2108 and confirm the presence of the other relic in the southwest with higher significance using uGMRT band-3. This new discovery places A2108 among the few low-mass clusters with double radio relics. The radio power of both the relics extrapolated to 1.4 GHz was found to be considerably low, making them outliers in the mass-luminosity plane. However, the non-axial X-ray shock positions, the significant size difference of NE (610 kpc \times 310 kpc) and SW (300 kpc \times 120 kpc) relics, their distinct morphologies, etc., helped us argue in favour of contrasting formation mechanism for these two relics.

Moreover, using the XMM-Newton science archive observation, we detect the presence of surface brightness jump and tentative temperature jump in the midst of the NE relic, indicating a weak shock ($\mathcal{M}_{\text{SB}} = 1.42^{+0.14}_{-0.14}$, $\mathcal{M}_{\text{T}} = 1.43^{+0.12}_{-0.02}$) usually disfavouring DSA origin for the relic. While the origin of the SW relic can be well justified from the passage of shock, the presence of multiple radio galaxies and the expanded structure of the NE relic suggest that the fossil electrons from radio galaxies play an important role in the generation of this source. Nevertheless, more clarity in understanding the underlying physical process of formation of these relics would need the information on the spectrum, requiring multi-frequency observations.

ACKNOWLEDGEMENTS

We thank IIT Indore for giving out the opportunity to carry out the research project. MR acknowledges support from the National Science and Technology Council of Taiwan (MOST 109-2112-M-007-037-MY3; NSTC 112-2628-M-007-003-MY3). This research is supported by DST-SERB through ECR/2017/001296 grant awarded to AD. RK acknowledges the support of the Department of Atomic Energy, Government of India, under project no. 12-R&D-TFR-5.02-0700 and from the SERB Women Excellence Award WEA/2021/000008. SP wants to thank the DST INSPIRE Faculty Scheme (code: IF-12/PH-44), during which the GLOMACS project was initiated. We thank the staff of the GMRT who have made these observations possible. The GMRT is run by the National Centre for Radio Astrophysics of the Tata Institute of Fundamental Research. This research made use of Astropy,³ a community-developed core Python package for Astronomy (Astropy Collaboration et al. 2013; and A. M. Price-Whelan et al. 2018), Matplotlib (Hunter 2007), and APLpy, an open-source plotting package for Python (Robitaille & Bressert 2012).

³ <http://www.astropy.org>

DATA AVAILABILITY

The data used for this work is available in the GMRT Online Archive (<https://naps.ncra.tifr.res.in/goa/data/search>) and XMM-Newton Science Archive (<http://nxsa.esac.esa.int/nxsa-web/#home>).

REFERENCES

- Astropy Collaboration et al., 2013, *A&A*, **558**, A33
- Bonafede A., et al., 2017, *MNRAS*, **470**, 3465
- Botteon A., Gastaldello F., Brunetti G., Dallacasa D., 2016, *MNRAS*, **460**, L84
- Botteon A., Brunetti G., Ryu D., Roh S., 2020, *A&A*, **634**, A64
- Botteon A., et al., 2022, *A&A*, **660**, A78
- Briggs D. S., 1995, in American Astronomical Society Meeting Abstracts. p. 112.02
- Brüggen M., van Weeren R. J., Röttgering H. J. A., 2012, *MNRAS*, **425**, L76
- Brunetti G., Jones T. W., 2014, *International Journal of Modern Physics D*, **23**, 1430007
- Caglar T., 2018, *MNRAS*, **475**, 2870
- Caprioli D., Spitkovsky A., 2014, *ApJ*, **783**, 91
- Chandra P., Ray A., Bhatnagar S., 2004, *ApJ*, **612**, 974
- Chatterjee S., Rahaman M., Datta A., Raja R., 2022, *AJ*, **164**, 83
- Crawford C. S., Allen S. W., Ebeling H., Edge A. C., Fabian A. C., 1999, *MNRAS*, **306**, 857
- Di Gennaro G., et al., 2021, *ApJ*, **911**, 3
- Dominguez-Fernandez P., Brüggen M., Vazza F., Banda-Barragan W. E., Rajpurohit K., Mignone A., Mukherjee D., Vaidya B., 2021, *MNRAS*, **500**, 795
- Drury L. O., 1984, *Advances in Space Research*, **4**, 185
- Duchesne S. W., Johnston-Hollitt M., Bartalucci I., Hodgson T., Pratt G. W., 2021a, *Publ. Astron. Soc. Australia*, **38**, e005
- Duchesne S. W., Johnston-Hollitt M., Wilber A. G., 2021b, *Publ. Astron. Soc. Australia*, **38**, e031
- Eckert D., Molendi S., Paltani S., 2011, *A&A*, **526**, A79
- Ensslin T. A., Biermann P. L., Klein U., Kohle S., 1998, *A&A*, **332**, 395
- Feretti L., Giovannini G., Govoni F., Murgia M., 2012, *A&ARv*, **20**, 54
- Gennaro G. D., et al., 2018, *The Astrophysical Journal*, **865**, 24
- Govoni F., Feretti L., Giovannini G., Böhringer H., Reiprich T. H., Murgia M., 2001, *A&A*, **376**, 803
- Hallman E. J., Alden B., Rapetti D., Datta A., Burns J. O., 2018, *ApJ*, **859**, 44
- Hoefl M., Brüggen M., 2007, *MNRAS*, **375**, 77
- Hogan M. T., et al., 2015, *Monthly Notices of the Royal Astronomical Society*, **453**, 1201–1222
- Hugoniot H., 1887, *Journal de Mathématiques Pures et Appliquées*, **3**, 477
- Hugoniot H., 1889, *J. Ec. Polytechnique*, **57**, 1
- Hunter J. D., 2007, *Computing in Science & Engineering*, **9**, 90
- HyeonHan K., et al., 2020, *ApJ*, **900**, 127
- Intema van der Tol, S. Cotton, W. D. Cohen, A. S. van Bemmelen, I. M. Röttgering, H. J. A. 2009, *A&A*, **501**, 1185
- Intema Jagannathan, P. Mooley, K. P. Frail, D. A. 2017, *A&A*, **598**, A78
- Jensen P. C., Pimblett K. A., 2012, *MNRAS*, **422**, 2841
- Jones A., et al., 2021, *MNRAS*, **505**, 4762
- Jones A., et al., 2023, *arXiv e-prints*, p. [arXiv:2301.07814](https://arxiv.org/abs/2301.07814)
- Kale R., Wik D. R., Giacintucci S., Venturi T., Brunetti G., Cassano R., Dallacasa D., de Gasperin F., 2017, *MNRAS*, **472**, 940
- Kang H., Ryu D., 2013, *ApJ*, **764**, 95
- Koribalski B. S., et al., 2023, *arXiv e-prints*, p. [arXiv:2304.11784](https://arxiv.org/abs/2304.11784)
- Lee W., Jee M. J., Kang H., Ryu D., Kimm T., Brüggen M., 2020, *ApJ*, **894**, 60
- Lee W., et al., 2022, *ApJ*, **924**, 18
- Locatelli N. T., et al., 2020, *MNRAS*, **496**, L48
- Molnar S. M., Hearn N. C., Stadel J. G., 2012, *ApJ*, **748**, 45
- Offringa A. R., Smirnov O., 2017, *MNRAS*, **471**, 301
- Paul S., Gupta P., Salunkhe S., Bhagat S., Sonkamble S., Hiray M., Dabhade P., Raychaudhury S., 2021, *MNRAS*, **506**, 5389
- Paul S., et al., 2023, *Journal of Astrophysics and Astronomy*, **44**, 38
- Planck Collaboration et al., 2014, *A&A*, **571**, A29
- Rahaman M., Raja R., Datta A., 2022, *MNRAS*, **509**, 5821
- Rajpurohit K., et al., 2022, *A&A*, **657**, A2
- Rankine W. J., 1870, *Philosophical Transactions of the Royal Society of London Series I*, **160**, 277
- Robitaille T., Bressert E., 2012, *APLpy: Astronomical Plotting Library in Python* (ascl:1208.017)
- Roettiger K., Burns J. O., Stone J. M., 1999, *ApJ*, **518**, 603
- Sanders J. S., Fabian A. C., Russell H. R., Walker S. A., Blundell K. M., 2016, *MNRAS*, **460**, 1898
- Scaife A. M. M., Heald G. H., 2012, *Monthly Notices of the Royal Astronomical Society: Letters*, **423**, L30
- Schellenberger G., et al., 2022, *ApJ*, **925**, 91
- Wen Z. L., Han J. L., 2013, *MNRAS*, **436**, 275
- Zhang C., Yu Q., Lu Y., 2014, *ApJ*, **796**, 138
- and A. M. Price-Whelan et al., 2018, *The Astronomical Journal*, **156**, 123
- de Gasperin F., van Weeren R. J., Brüggen M., Vazza F., Bonafede A., Intema H. T., 2014, *MNRAS*, **444**, 3130
- van Weeren R. J., Brüggen M., Röttgering H. J. A., Hoefl M., 2011a, *MNRAS*, **418**, 230
- van Weeren R. J., Hoefl M., Röttgering H. J. A., Brüggen M., Intema H. T., van Velzen S., 2011b, *A&A*, **528**, A38
- van Weeren R. J., et al., 2017, *Nature Astronomy*, **1**, 0005
- van Weeren R. J., de Gasperin F., Akamatsu H., Brüggen M., Feretti L., Kang H., Stroe A., Zandanel F., 2019, *Space Sci. Rev.*, **215**, 16
- van Weeren R. J., et al., 2021, *A&A*, **651**, A115

This paper has been typeset from a $\text{\TeX}/\text{\LaTeX}$ file prepared by the author.